

Original Research

3D virtual human atria: A computational platform for studying clinical atrial fibrillation

Oleg V. Aslanidi^{a,1}, Michael A. Colman^{a,1}, Jonathan Stott^a, Halina Dobrzynski^b, Mark R. Boyett^b, Arun V. Holden^c, Henggui Zhang^{a,d,*}

^a Biological Physics Group, School of Physics & Astronomy, University of Manchester, Manchester M13 9PL, UK

^b Faculty of Medical & Human Sciences, University of Manchester, Manchester M13 9NT, UK

^c Institute of Membrane and Systems Biology, and Multidisciplinary Cardiovascular Research Centre, University of Leeds, Leeds LS2 9JT, UK

^d School of Computer Science and Technology, Harbin Institute of Technology, Harbin, China

ARTICLE INFO

Article history:

Available online 7 July 2011

Keywords:

Virtual human atria

Sinoatrial node

Atrial fibrillation

Body surface ECG

ABSTRACT

Despite a vast amount of experimental and clinical data on the underlying ionic, cellular and tissue substrates, the mechanisms of common atrial arrhythmias (such as atrial fibrillation, AF) arising from the functional interactions at the whole atria level remain unclear. Computational modelling provides a quantitative framework for integrating such multi-scale data and understanding the arrhythmogenic behaviour that emerges from the collective spatio-temporal dynamics in all parts of the heart. In this study, we have developed a multi-scale hierarchy of biophysically detailed computational models for the human atria – the 3D virtual human atria. Primarily, diffusion tensor MRI reconstruction of the tissue geometry and fibre orientation in the human sinoatrial node (SAN) and surrounding atrial muscle was integrated into the 3D model of the whole atria dissected from the Visible Human dataset. The anatomical models were combined with the heterogeneous atrial action potential (AP) models, and used to simulate the AP conduction in the human atria under various conditions: SAN pacemaking and atrial activation in the normal rhythm, break-down of regular AP wave-fronts during rapid atrial pacing, and the genesis of multiple re-entrant wavelets characteristic of AF. Contributions of different properties of the tissue to mechanisms of the normal rhythm and arrhythmogenesis were investigated. Primarily, the simulations showed that tissue heterogeneity caused the break-down of the normal AP wave-fronts at rapid pacing rates, which initiated a pair of re-entrant spiral waves; and tissue anisotropy resulted in a further break-down of the spiral waves into multiple meandering wavelets characteristic of AF. The 3D virtual atria model itself was incorporated into the torso model to simulate the body surface ECG patterns in the normal and arrhythmic conditions. Therefore, a state-of-the-art computational platform has been developed, which can be used for studying multi-scale electrical phenomena during atrial conduction and AF arrhythmogenesis. Results of such simulations can be directly compared with electrophysiological and endocardial mapping data, as well as clinical ECG recordings. The virtual human atria can provide in-depth insights into 3D excitation propagation processes within atrial walls of a whole heart in vivo, which is beyond the current technical capabilities of experimental or clinical set-ups.

© 2011 Elsevier Ltd. All rights reserved.

1. Introduction

Atrial fibrillation (AF) is the most common sustained cardiac arrhythmia (Nattel et al., 2005). It annually affects a total of ~500,000 individuals in the UK alone, and the rate of hospitalization for AF and the cost of its treatment are increasing in epidemic proportions (Stewart et al., 2004; Anter et al., 2009). AF is

considered to be a major cause of morbidity and mortality: it can cause a reduction in cardiac output, predispose to heart failure and stroke, and increase sudden death rates (Benjamin et al., 1998; Anter et al., 2009). Although AF is a very costly public health problem, mechanisms underlying its genesis and control are incompletely understood, and its clinical treatments all have significant intrinsic limitations (Ehrlich and Nattel, 2009). Experimental animal studies

* Corresponding author. School of Physics & Astronomy, University of Manchester, Manchester M13 9PL, UK. Tel.: +44 161 306 3966.

E-mail address: henggui.zhang@manchester.ac.uk (H. Zhang).

¹ Joint first authors.

and clinical endocardial mapping have suggested that high-frequency irregular electrical activity in AF may be sustained by re-entrant wavelets propagating in an abnormal atrial tissue substrate (Harada et al., 1996; Jalife et al., 2002; Nattel et al., 2005). However, mechanisms underlying initiation of re-entry and the nature of the re-entrant substrate remain unclear.

It is believed that atrial tissues with substantial regional differences in intrinsic electrical properties are more susceptible to re-entry: the latter may result in conduction slowing and block in atrial tissue regions with longer refractoriness (Spach et al., 1989; Jalife et al., 2002; Nattel et al., 2005). Experimental data from animal cell and tissues indicate that both atria are characterized by significant regional differences in the action potential morphology and duration (APD), which are attributed to intrinsic variations in the ionic channel current densities and kinetics through the atria (Feng et al., 1998; Li et al., 2001; Sarmast et al., 2003). Similar heterogeneities in the APD have also been seen in human studies (Chen et al., 1999), although little data on regional heterogeneity of underlying ionic currents are available. Besides, clinical endocardial mapping studies and ECG data have shown heterogeneities in spatial distributions of the electrical excitation frequencies within the atria during AF (Haissaguerre et al., 1998; Sanders et al., 2005). However, an integrative approach to simultaneous studies of the ionic channel, action potential and conduction heterogeneities in the whole atria, and the resultant ECGs, is extremely difficult (if not impossible) to implement in an experimental or clinical set-up.

Thus, despite the availability of a considerable amount of experimental and clinical data on the heterogeneous ionic, cellular and tissue levels, the mechanisms of AF arising from the multi-scale functional interactions at the whole atria level remain unclear. Computational modelling provides a quantitative framework for integrating such multi-scale data and understanding the arrhythmogenic behaviour that emerges from the complex and collective spatio-temporal dynamics in all parts of the heart, across all scales and in various conditions (Rudy, 2000; Noble, 2002; Clayton et al., 2011). However, due to the lack of complete experimental datasets from human (as well as for the reasons of computational efficiency), existing models of the atria use either simplistic descriptions of the electrical properties or idealized tissue structure and anisotropy (Harrild and Henriquez, 2000; Seemann et al., 2006; Jacquemet et al., 2006; Ridler et al., 2006). Therefore, there is a need for efficient and quantitative atrial models that integrate data at all of ionic channel, cellular, anisotropic tissue and whole atria levels, which are validated against clinical data from humans.

In this study, we have constructed a hierarchy of models for human atrial cells and tissues, based on previously existing models (Courtemanche et al., 1998; Seemann et al., 2006; Kharche and Zhang, 2008), but substantially expanded to include (i) diffusion tensor MRI reconstruction of the human sinoatrial node (SAN) and right atrial (RA) tissue, (ii) anatomically detailed model of the entire heterogeneous atria and (iii) a human torso model simulating body surface ECGs. We demonstrate cross-scale relations between these models and the underlying experimental data. The developed 3D computational platform is used to study patterns of atrial conduction and mechanisms underlying the genesis of re-entrant AF associated with atrial spatial heterogeneity and anisotropy.

2. Methods

Station-temporal dynamics of electrical excitations in cardiac tissues can be described by the nonlinear partial differential equation (PDE) (Rudy, 2000; Clayton et al., 2011):

$$\frac{\partial V}{\partial t} = \nabla \cdot \tilde{\mathbf{D}} \nabla V - \frac{I_{\text{ion}}}{C_m} \quad (1)$$

Here V (mV) is the membrane potential, ∇ is a spatial gradient operator defined within the tissue geometry, and t is time (s). $\tilde{\mathbf{D}}$ is a tensor of diffusion coefficients ($\text{mm}^2 \text{ms}^{-1}$) that characterise electrotonic spread of voltage via gap junctional coupling, C_m (pF) is the cell membrane capacitance, and I_{ion} is the total membrane ionic current (pA). Note that when the diffusion term is neglected, Equation (1) becomes an ordinary differential equation describing excitation of a single cell.

2.1. Heterogeneous human atrial and sinoatrial node cell models

Families of electrophysiologically detailed cell models have been developed to describe the voltage- and time-dependent current, I_{ion} , in human atrial cells (Courtemanche et al., 1998; Nygren et al., 2001; Seemann et al., 2006; Maleckar et al., 2009) and in human SAN cells (Chandler et al., 2011). The models are based on voltage-clamp and mRNA expression datasets experimentally measured for individual ionic currents in various parts of the atria, and allow accurate simulations of the heterogeneous action potential (AP) morphologies.

In this study the human atrial AP model developed by Courtemanche et al. (1998) was modified based on voltage-clamp data showing large electrophysiological heterogeneity of the canine atria (Feng et al., 1998; Li et al., 2001). Primarily, conductances of the L-type Ca^{2+} current (I_{CaL}), transient outward K^+ current (I_{to}) and rapidly activated potassium current (I_{Kr}) were rescaled based on experimental data from dog (as described before by Seemann et al., 2006) to reproduce AP morphologies in various parts of the atria. Rescaled values of the conductances in the right (RA) and left (LA) atria, and bundles of the crista terminalis (CT) and pectinate muscles (PM) are summarized in Table 1. Note that due to lack of experimental data, the Bachmann's bundle (BB) is assumed to have same electrophysiology as the thick CT bundle. Table 1 also summarizes the resultant values of APD_{90} (AP duration at 90% repolarisation) measured in simulations of steady-state pacing of the RA, LA, CT and PM cells at the physiological cycle length of 700 ms. APs in these four cell types exhibit heterogeneous morphologies with significant differences in the plateau potential and APD, the latter ranging from 235 ms in the LA to 278 ms in the CT (Fig. 1A).

There is no biophysically-detailed model for the human SAN, which is due to the lack of relevant electrophysiological data. Therefore, for the human SAN, conductances of ionic currents in the Courtemanche et al. model were modified based on experimentally measured differences in ion channel mRNA expression between the RA and SAN in human as described previously (Chandler et al., 2011), resulting in feasible morphologies of spontaneous “pace-maker” APs (Fig. 1B).

2.2. Heterogeneous 3D anatomical model of human atria

The spatially heterogeneous 3D anatomical model of the atria (Fig. 1C) has been reconstructed by segmenting the Visible Female dataset (National Library of Medicine of the National Institute of Health, Bethesda, USA) in our previous study (Seemann et al., 2006). The 3D geometry has a spatial resolution of $0.33 \times 0.33 \times 0.33 \text{ mm}^3$. Primarily, specific atrial regions were segmented manually from the

Table 1
Current densities and APD (at 700 ms) in various regions of the human atria.

	RA	LA	CT/BB	PMs
I_{CaL} , nS/pF	0.1294	0.1294	0.2067	0.1238
I_{to} , nS/pF	0.1650	0.1650	0.2115	0.1650
I_{Kr} , nS/pF	0.0294	0.0470	0.0294	0.0294
APD_{90} , ms	266	235	278	262

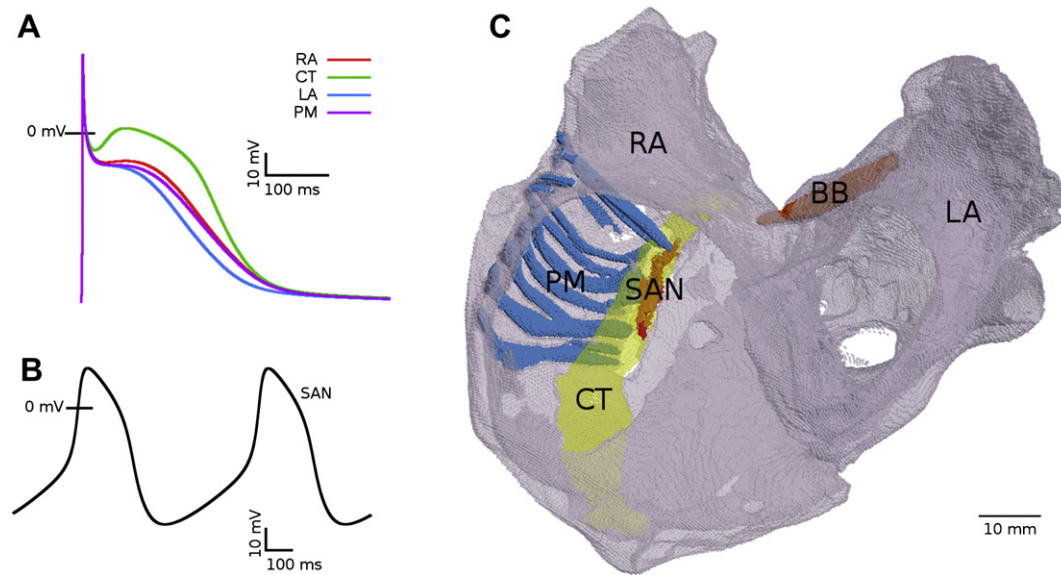


Fig. 1. Heterogeneous model of the human atria. A: AP profiles in the RA, LA, PM and CT cells at the cycle length of 700 ms. B: spontaneous APs in the SAN; C: 3D anatomical model of the human atria showing the main conductive bundles. Bulk atrial tissue in the LA and RA is anatomically homogeneous (translucent grey). The SAN and the major conductive bundles (CT, PM and BB) are coloured and marked by the respective abbreviations.

reconstructed atrial geometry based on well-established anatomic features. The RA and LA were separated, and the distinctive bundles of the CT, PMs and BB were identified (Fig. 1C). The SAN was reconstructed separately and merged with the atria (Section 2.5). Single cell models were mapped onto the respective regions of the 3D atrial tissue model.

Within the atria fibre orientation was introduced manually: the fibres were assumed aligned along the major atrial bundles – CT, PMs and BB. Values of the diffusion coefficients along and transverse to the fibres, $D_{||} = 1.0 \text{ mm}^2 \text{ ms}^{-1}$ and $D_{\perp} = 0.1 \text{ mm}^2 \text{ ms}^{-1}$ (which correspond to integral gap junctional conductances of 100 nS and 10 nS), were chosen to reproduce experimentally observed anisotropic AP conduction in the RA. Primarily, simulations of 3D atrial tissue model with such diffusion coefficients resulted in anisotropic conduction along the CT and in the RA wall with the velocities $v_{||} = 1.3 \text{ m s}^{-1}$ and $v_{\perp} = 0.7 \text{ m s}^{-1}$, respectively. Thus, the simulated anisotropy ratio was $v_{||}/v_{\perp} \approx 1.9$, in agreement with the respective experimental measurements of ~ 1.4 from the rabbit RA (Yamamoto et al., 1998) and 1.1–3.8 from human patients during atrial flutter (Liu et al., 2004). Note that the simulated values of the longitudinal and transverse conduction velocities, $v_{||}$ and v_{\perp} , are also in agreement with experimental data from humans (Boineau, 1985).

Thus, an anatomically and biophysically detailed, heterogeneous and anisotropic 3D model of the human atria (including the RA, LA, CT, PMs, BB and SAN) was constructed (Fig. 1).

2.3. DT-MRI reconstruction of the human SAN anatomy

Details of fibre architecture in cardiac tissue can be determined using a non-destructive method of diffusion tensor magnetic resonance imaging (DT-MRI). The method calculates the diffusion tensor for protons in the tissue from the signal attenuation and the intensity of magnetic gradient applied during a diffusion-weighted spin echo experiment (Basser et al., 1994). At each point within the tissue three principal directions of diffusion – along the fibre axis, perpendicular to the fibre axis in the sheet plane, and normal to the sheet plane – are given by the orthogonal eigenvectors \mathbf{f} , \mathbf{s} and \mathbf{n} of the diffusion tensor \mathbf{D} . The primary eigenvector, \mathbf{f} , has been validated as a measure of cardiac fibre orientation in the case of ventricular tissues (Hsu et al., 1998; Holmes et al., 2000).

We have used DT-MRI in order to reconstruct the tissue geometry and fibre orientation of the human SAN and the surrounding RA tissue; details of these experiments have been published elsewhere (Chandler et al., 2011). As a result, 60 contiguous DT-MRI images were acquired with 0.5 mm resolution between tissue slices and $0.25 \times 0.25 \text{ mm}^2$ resolution of each slice. In order to make resolution uniform in all three directions, a new slice was interpolated between each two adjacent slices, giving a dataset with $0.25 \times 0.25 \times 0.25 \text{ mm}^3$ voxel resolution. Image analysis of the dataset using DTI-Studio 2.4 (Laboratory of Brain Anatomical MRI and Center for Imaging Science at Johns Hopkins University, USA) allowed calculation of the diffusion tensor, \mathbf{D} , and its primary eigenvector, \mathbf{f} , for each voxel. Visualisation of the latter (Fig. 2) revealed a clear arrangement of fibres aligned along the CT and PM bundles of the RA, and a previously unknown loose pattern of fibres within the SAN. These distinct patterns of fibre orientations in the tissue have also been validated by histological experiments (Chandler et al., 2011). Resultant DT-MRI based tissue geometry and fibre orientation datasets were used to construct a detailed 3D computational model for the electrical pacemaking and AP conduction in the human SAN and the surrounding atrial tissue.

Single cell models for the SAN and RA were mapped onto the respective regions of the 3D SAN tissue model. Values of the diffusion coefficients along and transverse to the fibres were same as in the atrial model (Section 2.2), $D_{||} = 1.0 \text{ mm}^2 \text{ ms}^{-1}$ and $D_{\perp} = 0.1 \text{ mm}^2 \text{ ms}^{-1}$. However, both values were decreased 10-fold in the SAN in order to account for experimentally observed differences in Cx43 expression between the SAN and atrial tissues (Chandler et al., 2011). Combination of the coefficients, $D_{||}$ and D_{\perp} , with the primary eigenvector \mathbf{f} give the components of the tensor, \mathbf{D} , in Equation (1) for each voxel (Benson et al., 2008; Clayton et al., 2011).

The reconstructed 3D human SAN model with the detailed fibre orientation was integrated into the 3D model of the whole human atria (Section 2.5).

2.4. Torso model and body surface potentials

The ECG is the most common non-invasive method of monitoring the activity of the heart in a clinical environment by measuring the body surface potential (BSP) distribution. The latter

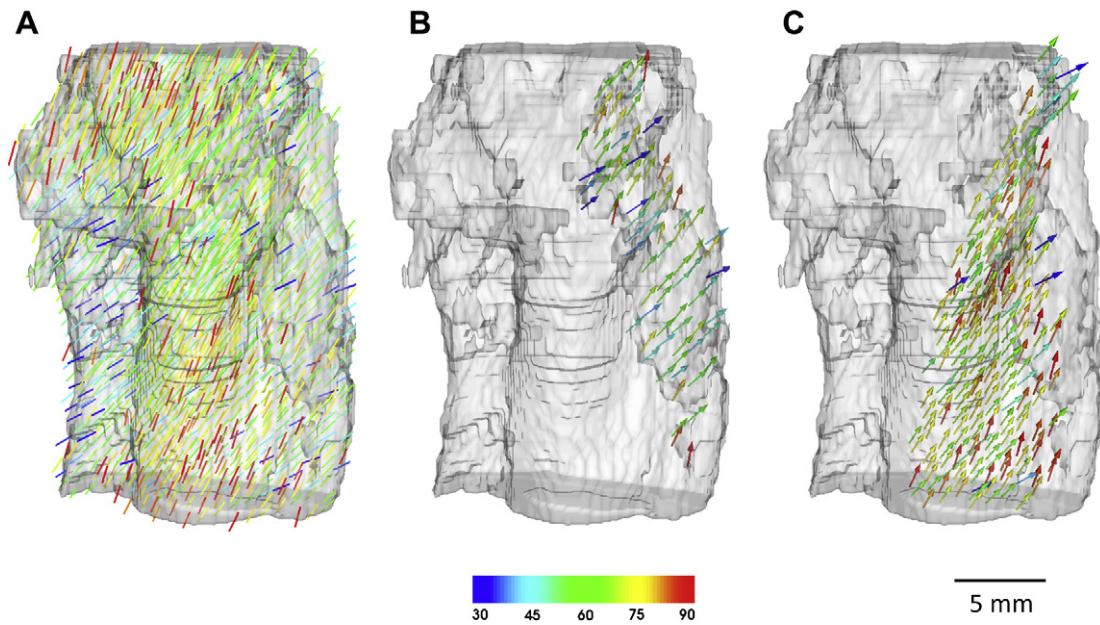


Fig. 2. Anatomical model of the human SAN. Tissue geometry (transparent grey) and fibre orientations (indicated by the direction as well as the colour of the arrows) are shown; the palette shows values of the fibre angle in respect to the horizontal plane (such that 90° corresponds to vertical fibres). A: The entire tissue comprising the SAN and surrounding atrium. B: SAN formed by loosely packed nodal cells. C: Atrial tissue in the area of CT – atrial cells are largely aligned along the CT and towards the SAN (adapted from Chandler et al. (2011)).

results from electrical current flows inside the torso and the heart associated with a propagating AP. The BSP can be simulated by solving the forward problem: mapping simulated voltage distributions on the heart surface into a torso model, and then simulating propagation of the electrical activity from the surface of the heart to the surface of the body (Barr et al., 1966). The latter involves solving Poisson's equation within the body using the boundary element method (Clayton and Holden, 2002).

The torso geometry (Fig. 3A) has been created previously (Weixue and Ling, 1996): it was derived from CT images of the human torso, and includes geometric representations for the lungs and the blood masses of the atria and ventricles. The 3D atrial model (see Section 2.1) was positioned within the torso based on the description of Ho and

Sanchez-Quintana (2009). First, the model was centred in the atrial co-ordinate system. Using the $z-x'-z''$ co-ordinate convention for Euler angles (which means that the angles are equivalent to three concatenated intrinsic rotations around changing axes z , x' and z'' , respectively; see in Goldstein, 1980) acting on the heart, the atrium was rotated by $(315^\circ, 135^\circ, 310^\circ)$. Following the rotation, a co-ordinate translation of $(-0.003 \text{ m}, -0.075 \text{ m}, -0.217 \text{ m})$ was applied to the atrium.

With the integrated 3D atria and torso model (see Section 2.5 below), BSP distribution on the torso surface was reconstructed using the boundary element method (Clayton and Holden, 2002). Several of the triangular elements on the torso surface were picked as the sites of the surface potential “electrodes”, with their locations

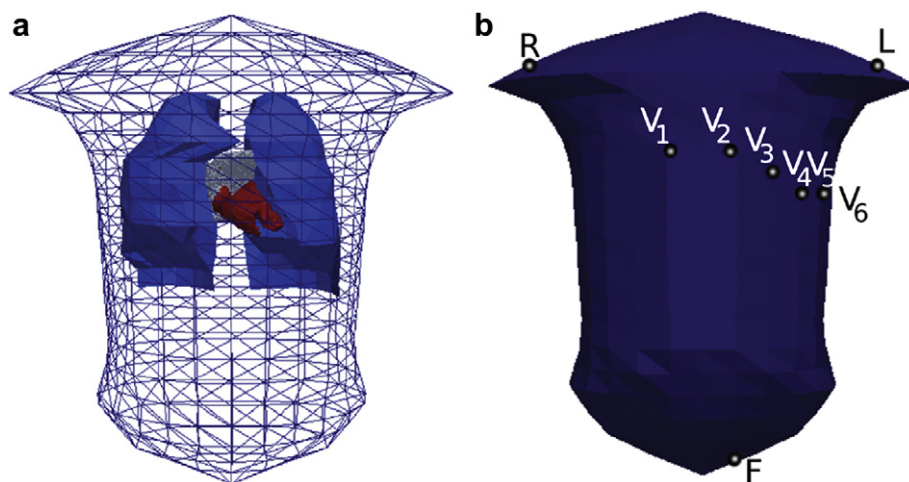


Fig. 3. Model of the human torso. A: The torso geometry used in the body surface potential simulations, shown here with the lungs (blue) and heart blood masses (red) within the surface mesh. B: Triangular elements selected as the positions of the electrodes used for deriving 12-lead ECGs. Lead potentials are defined as super-positions of the body surface potentials under the electrodes shown in (B): lead II = $F - R$, lead III = $F - L$, lead aVL = $L - (R + F)/2$, lead aVF = $F - (R + L)/2$.

shown in Fig. 3B. A standard 12-lead ECG – in case of the atria, twelve profiles of the P-wave corresponding to the atrial activation – was derived from the BSP time series. Correspondence between the locations of electrodes on the torso surface and the definitions of ECG leads used throughout the study is described in Fig. 3.

2.5. Integrating SAN, atrium and torso models

The 3D model of the human atria (Section 2.2) was completed by incorporation of the SAN model with the DT-MRI fibre reconstruction (Section 2.3), and placed within the torso model (Section 2.4). Note that the original SAN and atrial geometries had different resolutions ($0.5 \times 0.25 \times 0.25 \text{ mm}^3$ and $0.33 \times 0.33 \times 0.33 \text{ mm}^3$, respectively). To merge the two geometries together, resolution of the SAN dataset was rescaled to match that of the atrial dataset: 1) resolution of the SAN dataset was reduced to $0.5 \times 0.5 \times 0.5 \text{ mm}^3$ by neglecting every second grid node within every $0.25 \times 0.25 \text{ mm}^2$ slice; 2) two equidistant new nodes were interpolated between every two existing adjacent nodes, which resulted in a new geometry grid with resolution of $0.166 \times 0.166 \times 0.166 \text{ mm}^3$; 3) resolution was reduced to $0.33 \times 0.33 \times 0.33 \text{ mm}^3$ by neglecting every second node within the new grid.

Alignment of the CT and PM bundles between the atrial and SAN geometries (by co-ordinate rotation and translation of the latter) ensured correct positioning of the SAN within the RA. The fibre orientations in the SAN were then put through the same rotation and translation as the geometry itself and merged with the fibres introduced in the 3D atrial tissue bundles (Section 2.2). Primarily, DT-MRI based fibre orientations in the SAN and adjacent parts of the CT and PM replaced manually introduced fibre orientations in the respective parts of the atrial dataset; manual fibre orientations in the rest of the atrial dataset (for example, the entire BB) remained unchanged. Thus, an integrative model incorporating detailed electrical heterogeneity, tissue geometry and fibre orientation within the human atrium and SAN has been constructed and placed inside a torso model (Fig. 4). Each of the models within this multi-scale hierarchy was validated against available experimental data and used to study various aspects of electrical conduction in the human atria.

2.6. Numerical and computational methods

Equation (1) was solved numerically on the geometry grid using a finite-difference PDE solver based on the explicit Euler method

with time step $\Delta t = 0.005 \text{ ms}$, and the space steps Δx corresponding to the spatial resolutions of the tissue models used ($\Delta x = 0.33 \text{ mm}$ in the whole atria model and $\Delta x = 0.25 \text{ mm}$ in the standalone SAN model). We also ran test simulations with the space step in the atrial model scaled down to 0.25 mm (which corresponded to “shrinking” of the atria by $\sim 25\%$). Note that such a scaling down made the resolution of the atrial geometry similar to that of the SAN geometry, thus making the procedure of merging these two geometries (Section 2.5) more straightforward. The test simulations produced results qualitatively similar to those obtained with the space step of 0.33 mm , demonstrating stability of the model. Quantitatively, decreasing the space step from 0.33 to 0.25 mm resulted in very small ($<3\%$) changes of the computed AP conduction velocity values, which also demonstrates numerical convergence of the simulations (Section 4.3). Computer code implementing the PDE solver was parallelized under OpenMP and run on a 12-core Dell Precision T7500 desktop machine: simulations of 1 s of activity in the whole 3D heterogeneous atria took $\sim 2 \text{ h}$.

2.7. Initiation of AP propagation and re-entry

In the standalone 3D model of the atria (Section 2.2), several pacing protocols were applied to initiate AP propagation: (i) the tissue was stimulated in the presumed SAN area (superior part of the CT) at cycle length of 700 ms to simulate the normal rhythm (Protocol 1); (ii) the tissue was stimulated in the RA between the CT and PMs at cycle length of 230 ms to simulate a rapid atrial focus and the initiation of re-entry and AF (Protocol 2) – a similar protocol has been used previously to initiate re-entry in the rabbit RA model (Aslanidi et al., 2009); (iii) pacing Protocols 1 and 2 were applied simultaneously to simulate interactions between the normal rhythm and AF (Protocol 3).

In the integrated whole SAN-atria model (Section 2.5), APs were generated spontaneously due to the presence of the SAN pacemaker. Protocol 2 was applied to study interactions of the normal pacemaking and AF. In all protocols, each stimulus had an amplitude of 2 nA and duration of 2 ms .

3. Results

3.1. Simulated normal activation in the 3D atrial models

The 3D human atrial models without (Section 2.2) and with (Section 2.5) the integrated SAN are used to simulate the AP

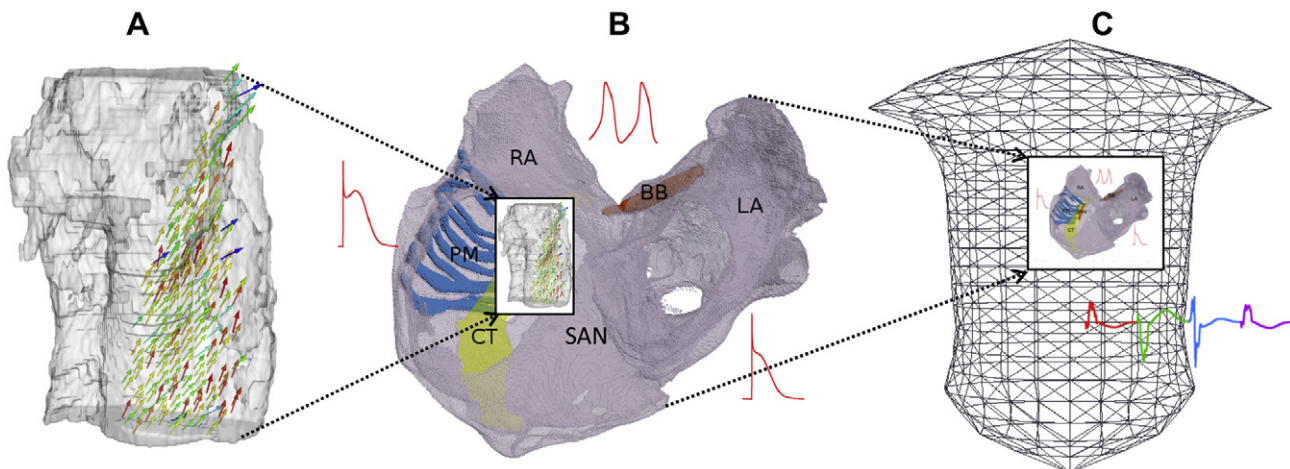


Fig. 4. Integration of the multi-scale models of the human atria. A: DT-MRI reconstruction of the geometry and fibre orientation the human SAN and surrounding RA can be integrated into B: 3D model of the whole atria, which can be incorporated into C: the torso model.

propagation through the atria. The resultant atrial activation sequences are (1) validated against results of detailed endocardial mapping in human patients (Lemery et al., 2007); (2) compared to each other in order to evaluate the effects of the SAN inclusion into the integrated model; (3) mapped inside the human torso model to simulate the BSPs and P-waves of the ECG, which are also compared between the two models. These simulations are illustrated in Fig. 5.

Activation pattern simulated using the 3D models without and with the SAN are shown in Fig. 5A(i) and B(i), respectively. In Fig. 5A(i), AP is initiated by pacing in the SAN area (Protocol 1, Section 2.7); in Fig. 5B(i), AP is generated spontaneously due to pacemaking SAN. In both cases, the AP is conducted rapidly down the CT and along the PM: the effect of the fibre orientation can be clearly seen in the earlier activations times along the CT in Fig. 5A(i) and B(i). The AP reaches the BB after 26 ms and rapidly spreads into the LA; it first evades the pulmonary vein (PV) region of the LA in 72 ms. Full activation of the RA is completed after 95 ms and full activation of the LA (and hence, both atria) is completed in 111 ms. These values are in a close agreement (see Table 2) with the high-resolution clinical mapping data (Lemery et al., 2007).

Table 2 gives a detailed summary of atrial activation times calculated using both models, and their comparisons with the experimental data by Lemery et al. (2007). It shows that integration

Table 2

Activation times in various regions of the atria in two models and experiment. SVC and IVC, superior and inferior vena cava; BB, Bachmann's bundle; RUPV and LIPV, right upper and left inferior pulmonary vein; RA and LA, right and left atrium.

	Atrial model without SAN	Atrial model with SAN	Experiment (Lemery et al.)
First SVC	18 ms	23 ms	26 ± 22 ms
First BB	26 ms	29 ms	31 ± 13 ms
First RUPV	72 ms	76 ms	75 ± 24 ms
First IVC	92 ms	86 ms	88 ± 33 ms
Latest RA	95 ms	92 ms	93 ± 17 ms
First LIPV	99 ms	102 ms	101 ± 23 ms
Latest LA	111 ms	118 ms	116 ± 18 ms

of the SAN further improves the agreement between the simulation results and mean experimental values of the activation times in major regions of the atria (note that these regions were chosen as they can be clearly identified based on their distinctive anatomical features). This may be explained by the fact that the SAN model includes detailed fibre orientation (primarily for parts of the RA), and hence, can simulate the activation sequence more accurately. Note also that in the model without the SAN the activation times are calculated from the moment of stimulation, whereas in the

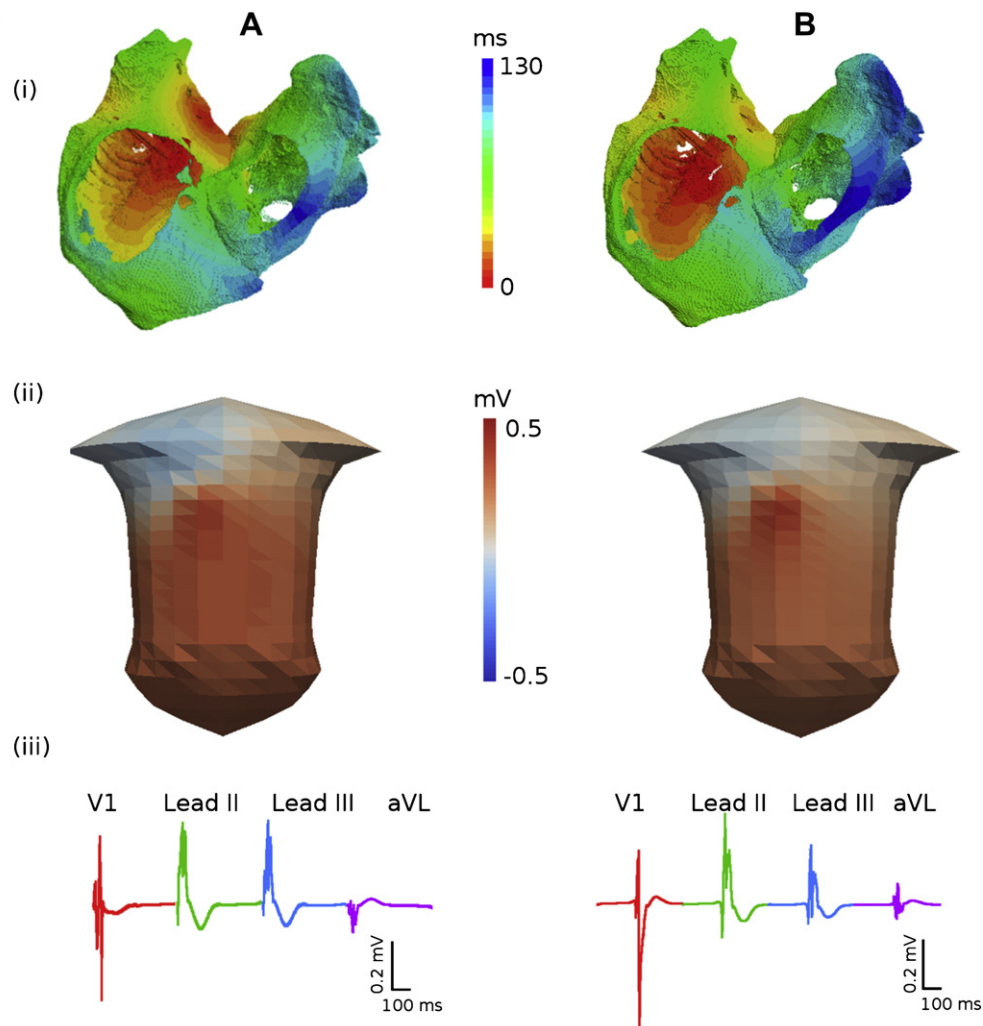


Fig. 5. Atrial activation sequence during sinus rhythm. A: Paced atrial model without the SAN. B: Atrial model with the pacemaking SAN. (i) Atrial activation times (measured as the time for a cell to reach the membrane potential of -60 mV); (ii) snapshots of the BSP distributions on the surface of the torso; (iii) P-waves in four representative ECG leads.

model with integrated SAN the times are calculated from the moment when the AP exits from the SAN. The calculated activation time of the SAN (from the spontaneous AP initiation to its slow exit into the RA) is 110 ms, which is close to the experimental value of 103 ms (Juillard et al., 1983).

Fig. 5 also shows BSPs corresponding to the AP propagation in the human atrial models without (Fig. 5A(ii)) and with (Fig. 5B(ii)) the SAN. The BSP distributions in both cases are qualitatively similar. AP conduction from the superior to the inferior CT results in a BSP wave which emerges over the lower right lung and propagates down towards the left leg, leaving a large positive region in the lower left torso and a negative region over the right shoulder (Fig. 5A(ii) and B(ii)). However, P-waves calculated from the BSPs for several ECG leads (Fig. 5A(iii) and B(iii)) exhibit small differences between the two models. Primarily, the P-wave in lead aVL is downward in the model without the SAN (Fig. 5A(iii)) and upward in the model with the SAN (Fig. 5B(iii)). The P-wave inversion in the model with the SAN is due to a small, but significant shift of the leading SAN pacemaking site in the inferior direction along the CT (Colman et al., 2011). Note that such a variety of P-waves morphologies has been observed in clinical ECG recordings (Mirvis, 1980): simulated P-wave morphologies are qualitatively similar to these data.

The simulations presented above demonstrate that 1) the 3D human atrial model reproduces activation patterns of the atria (as observed clinically during the normal rhythm by Lemery et al.

(2007) with good accuracy, 2) pacing of the standalone atrial model at a physiological rate provides a good approximation for the normal rhythm, 3) integration of the SAN model into the atrial model enables spontaneous pacemaking and improves agreement between the modelling and clinical data.

3.2. Transition from normal rhythm to AF

The developed 3D human atrial model with the integrated SAN is used to study the transition from normal sinus rhythm to re-entrant activation patterns characteristic of AF.

Fig. 6A(i) shows a regular electrical excitation wave on the epicardial surface of the atria during the normal rhythm with a period of ~700 ms. The excitation wave is first generated by the pacemaking SAN and then propagates through the RA (and later LA) maintaining a regular wave-front. Corresponding BSP and P-waves are shown in Fig. 6A(ii) and A(iii), respectively. A similar normal excitation pattern (“normal rhythm”) is observed in the case when the superior part of the CT is paced at 700 ms (Fig. 5A), with the wave propagation pattern on the epicardial surface, BSP and P-waves qualitatively similar to those shown in Fig. 6A.

However, rapid pacing of the 3D atrial model at the cycle length of 230 ms near the CT can result in a completely different pattern of wave propagation (Fig. 6B): after only three cycles of pacing, the wave-fronts are broken down, leading to multiple re-entrant

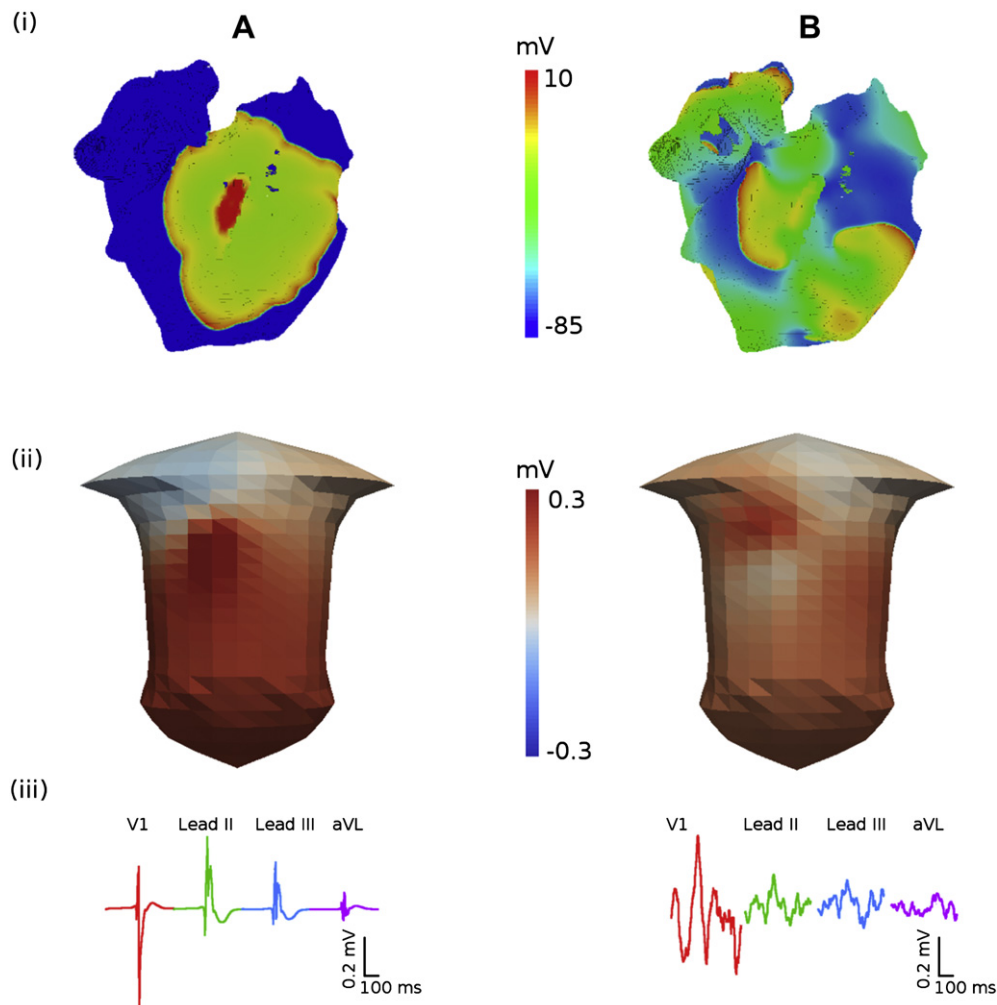


Fig. 6. Propagation patterns in the model of the human atria. A: Spontaneous normal rhythm. B: Pacing-induced AF. (i) snapshots of the membrane potential distribution on the epicardial surface of the atria; (ii) snapshots of the BSP in the torso; (iii) P-waves in four representative ECG leads.

wavelets propagating through the atria (Fig. 6B(i)). This is characteristic of electrical activation patterns observed in the atria during AF (Harada et al., 1996; Nattel et al., 2005). The BSP corresponding to the multiple re-entrant wavelets (Fig. 6B(ii)) is different from the one in the normal rhythm (Fig. 6A(ii)). The difference is clearly evident from the P-waves that show irregular “saw-tooth” morphologies (Fig. 6B(iii)) characteristic of AF (Fuster et al., 2006). Only P-waves in lead V₁ look similar to tachycardic “flutter waves”, which is also commonly seen in ECG recording from AF patients (Fuster et al., 2006). Note that AF patterns (as seen in Fig. 6B) can be simulated by both models with and without the SAN: in the case when the SAN is integrated into the atria, the rapidly (~ 4 Hz) rotating re-entrant wavelets suppress the relatively slow (~ 1.5 Hz) pacemaking by the SAN.

Under normal conditions, AF in these simulations is not sustained as re-entrant wavelets are self-terminated after ~ 1 s of rotation, after which the SAN restores its normal pacemaking rhythm. However, 2-fold reduction of the cell-to-cell coupling (i.e., the diffusion coefficients) in the model results in sustained AF: the irregular pattern of multiple re-entrant wavelets is maintained for the entire duration of simulations (10 s). This can be explained by the fact that the coupling reduction results in a decrease of the conduction velocity of wavelets, and hence, effectively increases the tissue substrate available for their rotation. Note that decreases of the atrial conduction velocity have been observed in AF patients (Kojodjojo et al., 2007), and the underlying coupling reduction can be due to structural remodelling of atrial tissue associated with AF (Everett et al., 2006).

AF in our simulations was initiated by rapid pacing in the RA close to the CT, which is in agreement with several experimental observations: transition from periodic waves to AF during rapid pacing of the sheep RA (Mandapati et al., 2000), clinically observed re-entrant circuits at the CT (Cox et al., 1991), and high incidence of dominant frequencies in the RA in patients with persistent AF (Sanders et al., 2005). Below we study the mechanisms of AF generation in the RA, primarily the role of RA tissue heterogeneity and anisotropy in the genesis of AF.

3.3. Mechanisms of AF initiation and development

The developed 3D human atrial model is used to dissect the mechanisms underlying the transition from rapid focal waves to re-entry and AF in the RA (Fig. 7). In simulation illustrated in Fig. 7, the RA is paced at the border between the CT and PM (Protocol 2, Section 2.7), where both the intrinsic APD difference and anisotropy of the bundles are pronounced. Primarily, the APD in the CT cells is longer (Table 1) and electrotonic coupling transverse to fibres of the CT is weak. Therefore, rapid pacing by three focal stimuli applied at the cycle length of 230 ms to the border between the CT and PM regions results in a conduction block of the third focal wave towards the CT (Fig. 7A). The broken wave spreads into the PMs and then the rest of RA (including the now-recovered CT), and after ~ 230 ms re-enters the initial pacing site from the superior and inferior CT directions. Hence, after ~ 700 ms of rapid pacing an almost-symmetric pair of re-entrant scroll waves are generated, which rotate in the RA and evade into the LA (Fig. 7A).

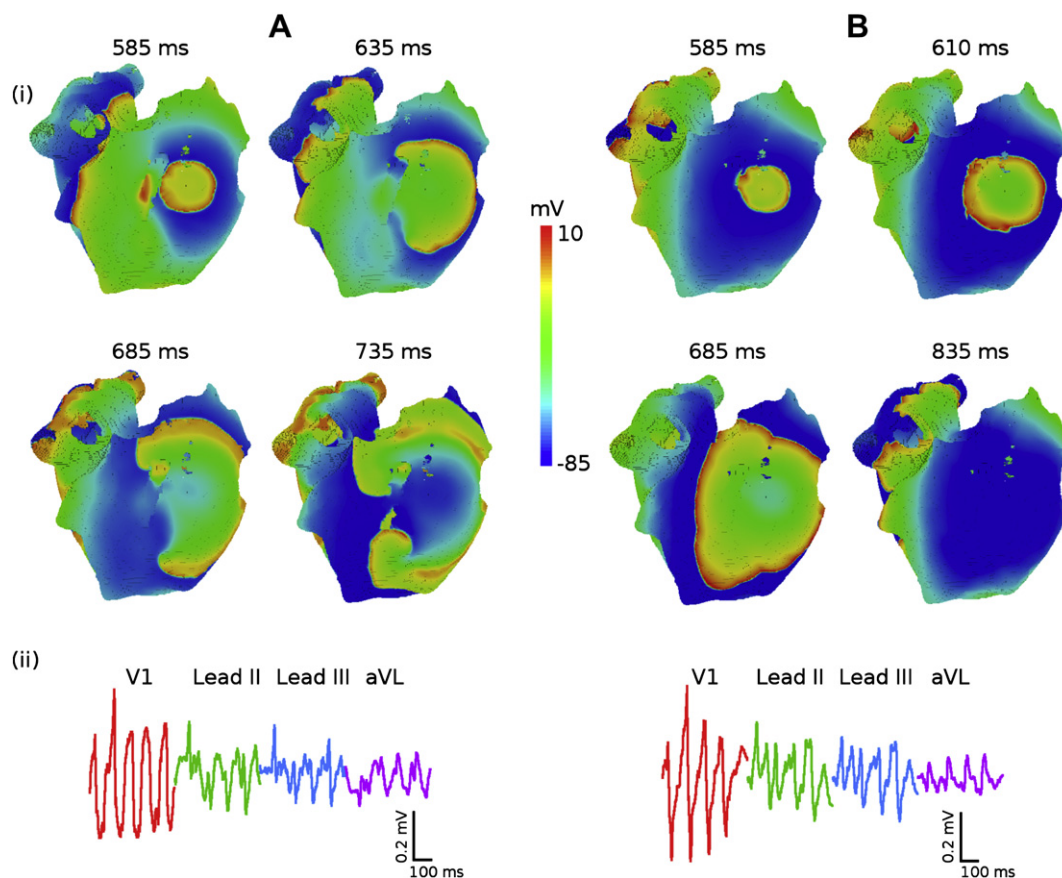


Fig. 7. Role of atrial heterogeneity in the initiation of re-entry. A: Re-entry in heterogeneous atria. B: Focal activity in homogeneous atria. In both A and B, the RA is paced at the cycle length of 230 ms between the CT and PMs. (i) snapshots of the potential distribution on the epicardial surface of the atria for successive moments of time; (ii) P-waves in four representative ECG leads.

Note that the short coupling (230 ms) between the successive focal waves is important for the re-entry initiation, as shown before for the rabbit RA (Aslanidi et al., 2009). Primarily, it 1) allows the high APD gradient between the CT and PM to be maintained and 2) results in conduction slowing of short-coupled waves, which gives sufficient time for the development of re-entry.

Further simulations suggest that both heterogeneity and anisotropy are also important for the re-entry initiation and development into the multi-wavelet state of AF. Fig. 7B illustrates that rapid pacing at any rate cannot generate re-entry in the homogeneous anisotropic RA (where all cells are assumed to have same electrophysiology as the RA cells). As there is no APD gradient between the CT and PM in this case, even short-coupled focal waves propagate in all directions without breaking their wave-fronts (Fig. 7B). The contribution of anisotropy to the initiation of re-entrant waves seems less important, as re-entry can still be initiated by rapid pacing in the heterogeneous isotropic RA (where the diffusion coefficient is assumed the same in all directions).

However, anisotropy contributes to breaking down of the initial re-entrant waves (Fig. 7A) into multiple wavelets characteristic of AF (Fig. 8). Fig. 8A(i) shows the pattern of electrical excitation on the epicardial surface of the 3D atrial model after 3 s of simulation. The pattern is very irregular, as several wavelets meander in different directions through changing re-entrant circuits. As before, P-waves show characteristic “saw-tooth” morphologies and “flutter waves” in lead V₁ (Fig. 8A(ii)). A similar simulation with heterogeneous isotropic RA model shows a much more regular excitation pattern (Fig. 8B(i)): the initial pair of re-entrant waves (seen in

Fig. 7A) is preserved, although it is not as symmetric as before due to irregularities of the tissue structure. Morphologies of P-waves in this case are also more regular, with clear peaks (Fig. 8B(ii)). Therefore, anisotropy of the RA bundles (such as the CT and PM) is important in the break-down of the initial pair of re-entrant waves, leading into multiple meandering wavelets characteristic of AF.

Thus, our simulations with the 3D human atrial model show that APD heterogeneity is important for the initial conduction block and generation of a pair of re-entrant waves (Fig. 7), whereas anisotropy of the RA bundles contributes to the symmetry breaking of the pair and genesis of multiple re-entrant wavelets and resultant “saw-tooth” P-waves (Fig. 8) seen in clinical AF.

4. Discussion

In this study, we have developed a multi-scale hierarchy of biophysically detailed computational models for the human atria, which is summarised in Fig. 4. Primarily, DT-MRI reconstruction of the tissue geometry and fibre orientation of the human SAN and surrounding RA (Fig. 4A) have been integrated into the 3D model of the whole atria based on the Visible Female dataset (Fig. 4B). The integrated anatomical model was combined with the heterogeneous AP models (Fig. 4B), and used to simulate the AP conduction in the human atria in various conditions: SAN pacemaking and atrial activation in the normal rhythm (Fig. 5), the genesis of multiple re-entrant wavelets and AF by rapid pacing (Fig. 6), and the effects of atrial heterogeneity and anisotropy (Figs. 7 and 8) on the development of AF. The 3D model of the atria itself has also been incorporated into the torso

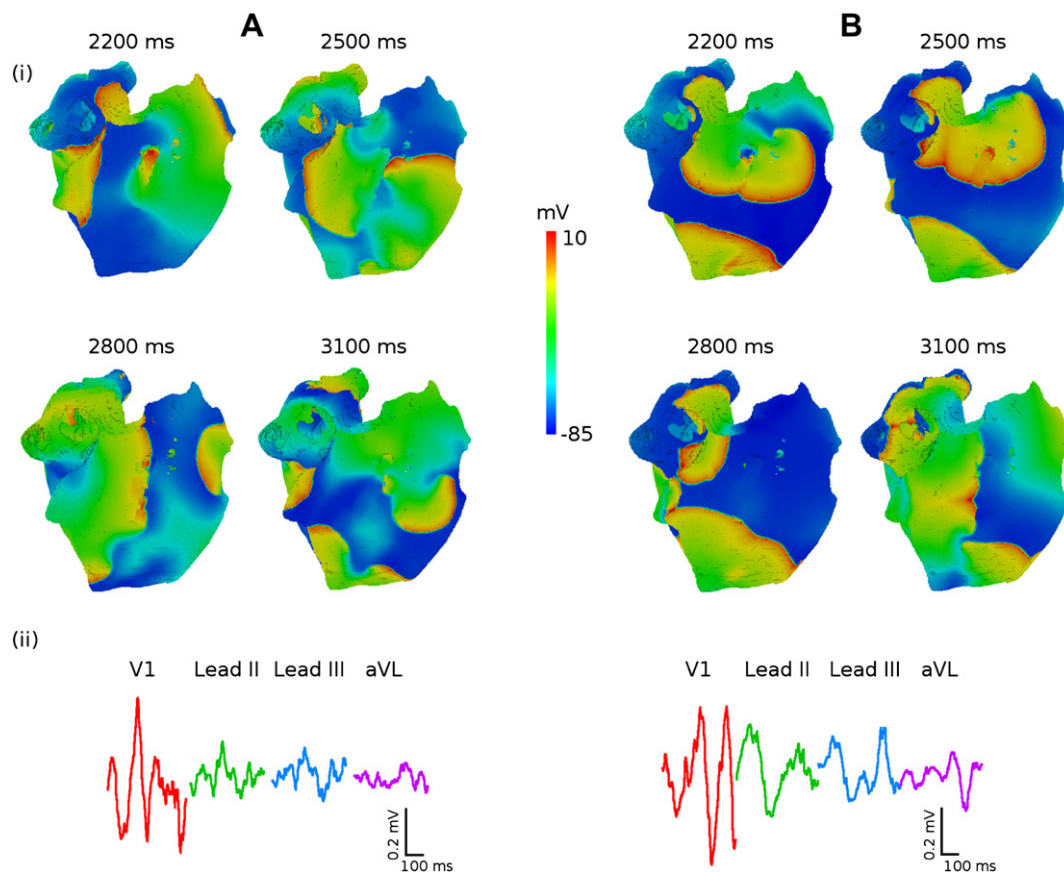


Fig. 8. Role of atrial anisotropy in the genesis of AF. A: Multiple meandering wavelets in anisotropic atria. B: Pair of re-entrant waves in isotropic atria. In both A and B, re-entry is initiated as shown in Fig. 7A. RA (i) snapshots of the potential distribution on the epicardial surface of the atria for successive moments of time; (ii) P-waves in four representative ECG leads. ECG in the anisotropic case A(ii) shows “flutter wave” in lead V₁ and “saw-tooth” morphologies in other leads, which are features of clinical AF. ECG in the isotropic case B(ii) shows P-waves with clear peaks.

model (Fig. 4C), and used to simulate the body surface ECG patterns in the normal and arrhythmic conditions (Figs. 5–7). Primarily, the torso model allows simulations of “saw-tooth” P-wave morphologies characteristic of clinical AF. Thus, a powerful computational platform for studying atrial conduction and arrhythmogenesis – the virtual human atria – has been developed. Below we discuss various components of the 3D virtual atria, their limitations, and interactions between them.

4.1. Model of the human SAN

Although several single cell and tissue models have been developed for the SAN in many animal species (Wilders, 2007), a model for the human SAN has been created only recently in our group (Chandler et al., 2011). This allowed us for the first time to incorporate the SAN model into the 3D model of the human atria and study the atrial activation due to the SAN pacemaking.

The SAN model based on DT-MRI reconstruction of the tissue geometry and detailed fibre orientation (Chandler et al., 2011) has several limitations. Thus, although the primary eigenvector of the diffusion tensor has been validated as a measure of the fibre orientation in tissue with a clear arrangement of densely packed long thin cells (such as atrial myocytes), there is no sufficient histological data to make such validation for areas formed by small spherical cells (SAN). However, our data provides evidence that diffusion is anisotropic not only in the atrium, but also in the SAN. First, as the three eigenvectors of the diffusion tensor are statistically different throughout the entire tissue (Chandler et al., 2011), the primary eigenvector can be used as a reliable measure of the fibre orientation in the tissue. Second, DT-MRI shows a clear arrangement of fibres in the SAN (Fig. 2B), and immunohistochemistry reveals a network of cells expressing gap-junction protein Cx43 (Chandler et al., 2011). Hence, the SAN contains clusters that can maintain diffusion between cells. As the fibre orientations were obtained from the SAN of a single human heart, additional experiments are needed to estimate the magnitude of biological variability in the fibre arrangement.

Although there are very limited data on AP properties of the SAN, APs generated by the model developed have realistic morphology and pacemaking rate (Fig. 1B), which is sufficient for simulating periodic AP generation and conduction into the RA (Fig. 5B): simulated epicardial activation sequence is similar to experimental data (Boineau et al., 1988; Lemery et al., 2007).

Besides, spatial heterogeneity within the SAN is important for the mechanisms of pacemaking (Zhang et al., 2000), but again there are no data from human SAN cells, primarily on 1) proportion and spatial distribution of central and peripheral cells, 2) differences in their electrophysiological properties, 3) shape and extent of electrical gradients in the ionic currents. Importantly, the lack of heterogeneity within the SAN does not affect its ability to drive the atrium – which is the primary subject of our study. Our preliminary simulations show that electrical gradients between the SAN centre and periphery can be introduced into the human SAN model based on the data from rabbit (Zhang et al., 2000); however, details of these of simulations are beyond the scope of this study.

4.2. Model of the human atria

We have developed a detailed 3D model of the human atria, which incorporates anatomical and electrophysiological heterogeneities (Fig. 4B). The atrial model can incorporate a smaller-scale model of the human SAN (Fig. 4A), and can be itself incorporated in a larger-scale model of the human torso (Fig. 4C). The resultant multi-scale model accurately simulates atrial activation patterns (Fig. 5), which are in good agreement with clinical mapping data by Lemery et al. (2007) (see in Table 2). Integration of the SAN model into the atrial

model not only enables spontaneous pacemaking, but also improves agreement between the model and clinical data (Table 2).

The model has been used for studying the mechanisms of AF arrhythmogenesis. Results of these simulations are discussed in detail below (Section 4.3). In simulations, rapid atrial pacing at the CT produced patterns of multiple re-entrant wavelets characteristic of AF (Figs. 6–8), which is in agreement with experimental observations (Cox et al., 1991; Mandapati et al., 2000). Morphologies of the corresponding ECG P-waves (Fig. 6B(iii)) showed irregular “saw-tooth” baseline and “flutter waves” in lead V₁, which are both features of clinical AF (Fuster et al., 2006).

Limitations of the 3D atrial model are largely inherited from the earlier models on which it was based. The Courtemanche et al. model was used here to simulate cellular APs of human atrial myocytes; the limitations of this model have been discussed elsewhere (Courtemanche et al., 1998; Nygren et al., 2001; Cherry et al., 2008). In the tissue model, intrinsic electrical heterogeneity and anisotropic intercellular coupling were introduced for several atrial regions phenomenologically (Seemann et al., 2006), due to the lack of detailed experimental data from human atria. For the electrical heterogeneity, the model used experimental data from dog (Feng et al., 1998; Li et al., 2001), whereas anisotropy parameters were introduced based on measurements from rabbit (Yamamoto et al., 1998). However, as mentioned above, the atrial activation sequence simulated with the resultant model was in close agreement quantitatively (see Table 2) with high-resolution mapping data accessing all parts of the atria (Lemery et al., 2007).

4.3. Spatial resolution

Spatial resolution of cardiac tissue models can be an important factor influencing both stability of the model and accuracy of numerical simulations (Clayton et al., 2011). The spatial resolution of $0.33 \times 0.33 \times 0.33 \text{ mm}^3$ used for the developed 3D human atrial model is based on the original resolution of Visible Female dataset (Seemann et al., 2006). In test simulations, the resolution was manually increased to $0.25 \times 0.25 \times 0.25 \text{ mm}^3$ (as done previously by Cherry and Evans, 2008), which effectively resulted in “shrinking” of the atria by ~25%. However, such a shrinking produced non-physiologically small atria. Therefore, in simulations used for studying a physiologically sized atria, the original space step $\Delta x = 0.33 \text{ mm}$ was used, and test simulations with the space step $\Delta x = 0.25 \text{ mm}$ were used only for checking the numerical convergence. The test simulations produced excitation patterns qualitatively similar to those obtained with the original resolution (as shown in Figs. 5–8), which demonstrates stability of the model. Quantitatively, decreasing the space step from 0.33 to 0.25 mm resulted in very small (<3%) changes of the simulated AP conduction velocity values, which also shows convergence of the numerical simulations. Note also that the space steps used are smaller than tissue space constants, which have been experimentally measured in the ranges 0.82–1.16 mm in atrial cells (Bonke, 1973) and 0.31–0.53 mm in the SAN cells (Bouman et al., 1989). Hence, any spatial heterogeneity that arises within the tissue due to the small numerical errors must be diminished by strong electrotonic interactions among cells.

Fenton et al. (2002) have also demonstrated the importance of spatial resolution in break-down of scroll waves in anisotropic tissues with fibre rotation. Such a break-down can occur if spatial resolution is too coarse and cell-to-cell coupling is too low. Primarily, the scroll wave break-down has occurred when the diffusion coefficients had very small values of $\sim 0.0001 \text{ mm}^2 \text{ ms}^{-1}$; when the same simulation has been performed using larger diffusion coefficients, the scroll waves were stable (Fenton et al., 2002). The smallest diffusion coefficient used in the anisotropic 3D human atrial model (D_{\perp} in the SAN region) was $0.01 \text{ mm}^2 \text{ ms}^{-1}$, which is ~100 times higher than that

used by Fenton et al. to produce the break-down. Therefore, the scroll wave initiation and break-down seen in the present simulations of the 3D atrial model (Figs. 7 and 8) are unlikely due to the same mechanisms as reported by Fenton et al. However, they are similar to those described by Aslanidi et al. (2009): break-down of the normal excitation wave-fronts into re-entry occurred due to the APD differences between the CT and PM regions (Fig. 7). Note that scroll waves were initiated in both anisotropic (Fig. 8A) and isotropic (Fig. 8B) atrial models, and hence, the fibre orientation cannot be responsible for the initial break-down. Note also that results by Aslanidi et al. have been based on a rabbit atrial tissue model with the resolution of $0.04 \times 0.04 \times 0.04 \text{ mm}^3$: qualitative similarities between results obtained using the model with such a fine resolutions (Aslanidi et al., 2009) and results of the present study (Fig. 7) provide additional validation to the latter.

Further break-down of the initial pair of scroll waves into AF state occurred only in the anisotropic 3D human atrial model (Fig. 8A). Although the diffusion coefficient used in these simulations was ~ 100 larger than that used by Fenton et al. (2002) to produce the scroll break-down, there is a possibility that a similar mechanism may be involved. Simulations of models with finer spatial resolution will ultimately be required to check this. Note, however, that such fine-resolved models can only be obtained by interpolation of the existing tissue geometries (which itself can lead to artefacts), and at the expense of exponential increases in the required computing resources.

4.4. Comparison to other models

Several 3D models of the human atria have been constructed before (Harrild and Henriquez, 2000; Seemann et al., 2006; Jacquemet et al., 2006; Cherry and Evans, 2008); most of them were based on the single cell description of Courtemanche et al. (1998) and the Visible Female geometry dataset. While these models included various details of atrial anatomy and electrophysiology, each of these studies had certain limitations. Anisotropic 3D model by Harrild and Henriquez (2000) did not include electrophysiological heterogeneities of the human atria, and only studied normal atrial activation. Seemann et al. (2006) included such heterogeneities, but their model of the SAN was idealised, and the simulated atrial activation sequence showed limited agreement with experimental data; besides, they did not consider AF. Jacquemet et al. (2006) considered a detailed 3D model with MRI-based atrial geometry, and studied initiation of AF-like state by rapid atrial pacing, similar to our study. However, in order to obtain such AF, Jacquemet et al. introduced patchy non-physiological heterogeneities throughout the atria, which had no relation to naturally existing electrophysiological heterogeneities in human atria. Finally, Cherry and Evans (2008) used the model by Harrild and Henriquez to simulate re-entrant scroll waves, and observed transient break-ups of the scrolls into multiple wavelets. However, their models did not consider electrical heterogeneity in the atria, and the original scroll wave was initiated by an appropriately timed cross-field stimulation. We believe our 3D model of the human atria overcomes many limitations of those earlier models by considering not only detailed atrial anatomy and electrophysiology, but also accurate regional heterogeneity and anisotropy. Primarily, the latter two features enable simulations of AF arrhythmogenesis without using any idealised heterogeneities or stimulation protocols.

4.5. Mechanisms of AF

Experimental animal studies and clinical mapping data have suggested that high-frequency irregular electrical activity in AF may be sustained by re-entrant wavelets propagating in an abnormal atrial

tissue substrate (Harada et al., 1996; Jalife et al., 2002; Nattel et al., 2005). Atrial tissues with large regional differences in electrical properties are more susceptible to re-entry, which may result from conduction slowing in atrial tissue regions with long refractoriness or high conduction anisotropy (Allessie et al., 1976; Spach et al., 1989; Aslanidi et al., 2009). Multiple experimental and clinical results have also suggested that “driver” regions acting as high-frequency sources during AF may be located in the LA, whereas the RA is characterised by heterogeneous electrical activity and multiple wavelets (Haissaguerre et al., 1998; Chen et al., 1999; Sanders et al., 2005). The origin of such multiple wavelets is unclear; our simulations of the break-down of excitation wave-fronts in the heterogeneous RA bundles may provided new insights into the mechanisms of their generation.

The basis for LA predominance of AF is also unknown. Myocardial sleeves of the PVs in the LA are recognized as important sources of ectopic electrical activity – ablation of the PV-LA junctions to electrically isolate PVs from the LA can terminate AF (Haissaguerre et al., 1998; Chen et al., 1999). However, knowledge of the arrhythmogenic substrate in the PVs is limited. Hence, the 3D atrial model can benefit from incorporation of the PV model, which is subject to availability of experimental data from human or electrophysiologically similar large animal species. As junctions between the LA and PV are characterized by high electrical heterogeneity and anisotropy (Chen et al., 1999; Arora et al., 2003), they may provide a substrate for the generation of re-entry from ectopic beats – via mechanisms similar to those reported in this study for the CT-PM junctions.

Rapid AF is also often progressive, going from paroxysmal to persistent to permanent, with electrical and structural remodelling of the atria leading to a substrate that facilitates self-perpetuation of the arrhythmia (Nattel et al., 2005; Anter et al., 2009). Hence, the effects of remodelling should be incorporated into the model, primarily changes of the ionic channel current densities (e.g., Ehrlich and Nattel, 2009) and in atrial tissue structure (such as atrial fibre disarray, fibrosis and hypertrophy, Everett et al., 2006). Remodelling due to rapid electrical activity is not the only mechanism of AF self-perpetuation: under AF conditions, the acetylcholine-activated current, $I_{K_{ACh}}$, can become constitutively active even in the absence of vagal tone – and hence, when enhanced by vagal stimulation, can further promote AF (Sarmast et al., 2003; Katsouras et al., 2009). A wide variety of mechanisms that may be involved in the genesis of AF require further studies.

4.6. Model of the human torso

The 3D atrial model was incorporated into the torso model (Fig. 4C), and used to simulate the body surface ECGs in the normal (Fig. 5) and abnormal (Fig. 6) conditions. This allowed us to simulate “saw-tooth” P-wave morphologies consistent with clinical AF data (Fuster et al., 2006).

Note that P-waves in some leads exhibit ‘notched’ morphologies even in normal conditions, as opposed to smoother P-waves seen in clinical recordings. This may be due to the simplistic torso geometry and omission of several inhomogeneities within the torso. Inclusion of such structures as the skeletal muscle (which is electrically excitable) may contribute to a smoothing of the P-waves. However, this would require the use of the finite element method, which is more computationally costly than the boundary element method (Clayton and Holden, 2002). Note also that even clinically recorded P-wave morphologies are not necessarily smooth (Mirvis, 1980).

4.7. Conclusions

Understanding the spatio-temporal patterns of propagation in the atria during normal sinus rhythm, how it changes with rate, and

the genesis of atrial arrhythmias (such as AF) requires full in-depth access to cells and tissue, and the possibility to control individual variables. This is extremely difficult (if not impossible) to implement in an experimental or clinical set-up. The 3D virtual human atria, based on detailed ionic channel and cell electrophysiology, and histology and DT-MRI based anatomy, gives a validated means for dissecting and explaining propagation in the normal and arrhythmic atria. Results of the model simulations can be compared with the clinical mapping data and ECG recordings, providing additional validation. Although, due to the lack of experimental detail from human, the model currently lacks some components (such as description of the PV), these can be incorporated in the already built-up platform when more data become available.

In summary, our virtual atrial model is a state-of-the-art complementary tool for investigating the multi-scale dynamical behaviour in the human atria during the normal rhythm and AF.

Editors' note

Please see also related communications in this issue by Bordas et al. (2011) and Konukoglu et al. (2011).

Acknowledgements

This work was supported by grants from the **Engineering and Physical Sciences Research Council (EP/I029826/1)**, British Heart Foundation (PG/10/69/28524) and Wellcome Trust (WT/081809/Z/06/Z).

References

- Allessie, M.A., Bonke, F.I., Schopmann, F.T.G., 1976. Circus movement in rabbit atrial muscle as a mechanism of tachycardia. II. The role of nonuniform recovery of excitability in the occurrence of unidirectional block studied with multiple microelectrodes. *Circ. Res.* 39, 168–177.
- Anter, E., Jessup, M., Callans, D.J., 2009. Atrial fibrillation and heart failure: treatment considerations for a dual epidemic. *Circulation* 119, 2516–2525.
- Aslanidi, O.V., Boyett, M.R., Dobrzynski, H., Li, J., Zhang, H., 2009. Mechanisms of transition from normal to re-entrant electrical activity in a model of rabbit atrial tissue: interaction of tissue heterogeneity and anisotropy. *Biophys. J.* 96, 798–817.
- Arora, R., Verheule, S., Scott, L., et al., 2003. Arrhythmogenic substrate of the pulmonary veins assessed by high-resolution optical mapping. *Circulation* 107, 1816–1821.
- Basser, P.J., Mattiello, J., LeBihan, D., 1994. Estimation of the effective self-diffusion tensor from the NMR spin echo. *J. Magnet Res. Med.* 30, 201–206.
- Barr, R.C., Pilkington, T.C., Boineau, J.P., Spach, M.S., 1966. Determining surface potentials from current cipoles with application to electrocardiography. *IEEE Trans. Biomed. Eng.* 13, 88–92.
- Benjamin, E.J., Wolf, P.A., D'Agostino, R.B., Silbershatz, H., Kannel, W.B., Levy, D., 1998. Impact of atrial fibrillation on the risk of death: the Framingham heart study. *Circulation* 98, 946–952.
- Benson, A.P., Aslanidi, O.V., Zhang, H., Holden, A.V., 2008. The canine virtual ventricular wall: a platform for dissecting pharmacological effects on propagation and arrhythmogenesis. *Prog. Biophys. Mol. Biol.* 96, 187–208.
- Boineau, J.P., 1985. Atrial flutter: a synthesis of concepts. *Circulation* 72, 249–257.
- Boineau, J.P., Canavan, T.E., Schuessler, R.B., Cain, M.E., Corr, P.B., Cox, J.L., 1988. Demonstration of a widely distributed atrial pacemaker complex in the human heart. *Circulation* 77, 1221–1237.
- Bonke, F.I.M., 1973. Passive electrical properties of atrial fibers of the rabbit heart. *Pflügers Arch.* 339, 1–15.
- Bordas, R., Gillow, K., Lou, Q., Efimov, I.R., Gavaghan, D., Kohl, P., Grau, V., Rodriguez, B., 2011. CBG: rabbit-specific ventricular model of cardiac electrophysiological function including specialized conduction system. *Prog. Biophys. Mol. Biol.* 107, 90–100.
- Bouman, L.N., Duivenvoorden, J.J., Bukeauskas, F.F., Jongsma, H.J., 1989. Anisotropy of electrotonus in the sinoatrial node of the rabbit heart. *J. Mol. Cell Cardiol.* 21, 407–418.
- Chandler, N.J., Aslanidi, O.V., Buckley, D.L., et al., 2011. Computer three-dimensional anatomical reconstruction of the human sinus node and a novel paranodal area. *Anat. Rec.* 294, 970–979.
- Chen, S.A., Hsieh, M.H., Tai, C.T., et al., 1999. Initiation of atrial fibrillation by ectopic beats originating from the pulmonary veins: electrophysiological characteristics, pharmacological responses, and effects of radiofrequency ablation. *Circulation* 100, 1879–1886.
- Cherry, E.M., Evans, S.J., 2008. Properties of two human atrial cell models in tissue: restitution, memory, propagation, and reentry. *J. Theor. Biol.* 254, 674–690.
- Cherry, E.M., Hastings, H.M., Evans, S.J., 2008. Dynamics of human atrial cell models: restitution, memory, and intracellular calcium dynamics in single cells. *Prog. Biophys. Mol. Biol.* 98, 24–37.
- Clayton, R.H., Holden, A.V., 2002. Computational framework for simulating the mechanisms and ECG of re-entrant ventricular fibrillation. *Physiol. Meas.* 23, 707–726.
- Clayton, R.H., Bernus, O., Cherry, E.M., et al., 2011. Models of cardiac tissue electrophysiology: progress, challenges and open questions. *Prog. Biophys. Mol. Biol.* 104, 22–48.
- Colman, M.A., Aslanidi, O.V., Stott, J., Holden, A.V., Zhang, H., 2011. Correlation between P-wave morphology and origin of atrial focal tachycardia – insights from realistic models of the human atria and torso. *IEEE Trans. Biomed. Eng.* doi:10.1109/TBME.2011.2161305.
- Cox, J.L., Canavan, T.E., Schuessler, R.B., et al., 1991. The surgical treatment of atrial fibrillation. II: intraoperative electrophysiologic mapping and description of the electrophysiologic basis of atrial flutter and atrial fibrillation. *J. Thorac. Cardiovasc. Surg.* 101, 406–426.
- Courtemanche, M., Ramirez, R.J., Nattel, S., 1998. Ionic mechanisms underlying human atrial action potential properties: insights from a mathematical model. *Am. J. Physiol.* 275, H301–H321.
- Ehrlich, J.R., Nattel, S., 2009. Novel approaches for pharmacological management of atrial fibrillation. *Drugs* 69, 757–774.
- Everett, T.H., Wilson, E.E., Verheule, S., Guerra, J.M., Foreman, S., Olgin, J.E., 2006. Structural atrial remodeling alters the substrate and spatiotemporal organization of atrial fibrillation: a comparison in canine models of structural and electrical atrial remodeling. *Am. J. Physiol.* 291, H2911–H2923.
- Feng, J., Yue, L., Wang, Z., Nattel, S., 1998. Ionic mechanisms of regional action potential heterogeneity in the canine right atrium. *Circ. Res.* 83, 541–551.
- Fenton, F.H., Cherry, E.M., Hastings, H.M., Evans, S.J., 2002. Multiple mechanisms of spiral wave breakup in a model of cardiac electrical activity. *Chaos* 12, 852–892.
- Fuster, V., Ryden, L.E., Cannom, D.S., et al., 2006. ACC/AHA/ESC 2006 guidelines for the management of patients with atrial fibrillation. *Circulation* 114, e257–e354.
- Goldstein, H., 1980. *Classical Mechanics*. Addison-Wesley, Reading, MA, pp. 143–148.
- Haissaguerre, M., Jais, P., Shah, D.C., et al., 1998. Spontaneous initiation of atrial fibrillation by ectopic beats originating in the pulmonary veins. *N. Engl. J. Med.* 339, 659–666.
- Harada, A., Sasaki, K., Fukushima, T., et al., 1996. Atrial activation during chronic atrial fibrillation in patients with isolated mitral valve disease. *Ann. Thorac. Surg.* 61, 104–111.
- Harrild, D., Henriquez, C., 2000. A computer model of normal conduction in the human atria. *Circ. Res.* 87, 25–36.
- Ho, S.Y., Sanchez-Quintana, D., 2009. The importance of atrial structure and fibers. *Clin. Anat.* 22, 52–63.
- Holmes, A.A., Scollan, D.F., Winslow, R.L., 2000. Direct histological validation of diffusion tensor MRI in formaldehyde-fixed myocardium. *J. Magnet Res. Med.* 44, 157–161.
- Hsu, E.W., Muzikant, A.L., Matulevicius, S.A., Penland, R.C., Henriquez, S.C., 1998. Magnetic resonance myocardial fiber-orientation mapping with direct histological correlation. *Am. J. Physiol.* 274, H1627–H1634.
- Jalife, J., Berenfeld, O., Mansour, M., 2002. Mother rotors and fibrillatory conduction: a mechanism of atrial fibrillation. *Cardiovasc. Res.* 54, 204–216.
- Jacquemet, V., van Oosterom, A., Vesin, J.-M., Kappenberger, L., 2006. Analysis of electrocardiograms during atrial fibrillation. A biophysical model approach. *IEEE Eng. Med. Biol. Mag.* 25, 79–88.
- Juillard, A., Guillemin, F., Chuong, H.V., Barrillon, A., Gerbaux, A., 1983. Sinus node electrogram recording in 59 patients. Comparison with simultaneous estimation of sinoatrial conduction using premature atrial stimulation. *Br. Heart J.* 50, 75–84.
- Katsouras, G., Sakabe, M., Comtois, P., et al., 2009. Differences in atrial fibrillation properties under vagal nerve stimulation versus atrial tachycardia remodeling. *Heart Rhythm* 6, 1465–1472.
- Kharche, S., Zhang, H., 2008. Simulating the effects of atrial fibrillation induced electrical remodeling: a comprehensive simulation study. *Conf. Proc. IEEE Eng. Med. Biol. Soc.* 1, 593–656.
- Kojodjojo, P., Peters, N.S., Davies, D.W., Kanagaratnam, P., 2007. Characterization of the electroanatomical substrate in human atrial fibrillation: the relationship between changes in atrial volume, refractoriness, wavefront propagation velocities, and AF burden. *J. Cardiovasc. Electrophysiol.* 18, 269–275.
- Konukoglu, E., Relan, J., Cilingir, U., Menze, B.H., Chinchapatnam, P., 2011. Probabilistic model personalization using an efficient framework: application to Eikonal-diffusion models in cardiac electrophysiology. *Prog. Biophys. Mol. Biol.* 107, 134–146.
- Lemery, R., Birnie, D., Tang, A.S., Green, M., Gollob, M., Hendry, M., Lau, E., 2007. Normal atrial activation and voltage during sinus rhythm in the human heart: an endocardial and epicardial mapping study in patients with a history of atrial fibrillation. *J. Cardiovasc. Electrophysiol.* 18, 402–408.
- Li, D., Zhang, L., Kneller, J., Nattel, S., 2001. Potential ionic mechanism for repolarization differences between canine right and left atrium. *Circ. Res.* 88, 1168–1175.
- Liu, T.Y., Tai, C.T., Huang, B.H., et al., 2004. Functional characterization of the crista terminalis in patients with atrial flutter: implications for radiofrequency ablation. *J. Am. Coll. Cardiol.* 43, 1639–1645.

- Maleckar, M.M., Greenstein, J.L., Giles, W.R., Trayanova, N.A., 2009. K^+ current changes account for the rate dependence of the action potential in the human atrial myocyte. *Am. J. Physiol.* 297, H1398–H1410.
- Mandapati, R., Skanes, A., Chen, J., Berenfeld, O., Jalife, J., 2000. Stable micro-reentrant sources as a mechanism of atrial fibrillation in the isolated sheep heart. *Circulation* 101, 194–199.
- Mirvis, D.M., 1980. Body surface distribution of electrical potential during atrial depolarization and repolarization. *Circulation* 62, 167–173.
- Nattel, S., Shiroshita-Takeshita, A., Brundel, B.J., Rivard, L., 2005. Mechanisms of atrial fibrillation: lessons from animal models. *Prog. Cardiovasc. Dis.* 48, 9–28.
- Noble, D., 2002. Modeling the heart – from genes to cells to the whole organ. *Science* 295, 1678–1682.
- Nygren, A., Leon, L.J., Giles, W.R., 2001. Simulations of the human atrial action potential. *Phil Trans. Royal Soc. A* 359, 1111–1125.
- Ridler, M., McQueen, D.M., Peskin, C.S., Vigmond, E., 2006. Action potential duration gradient protects the right atrium from fibrillating. *Conf. Proc. IEEE Eng. Med. Biol. Soc.* 1, 3978–3981.
- Rudy, Y., 2000. From genome to physiome: integrative models of cardiac excitation. *Ann. Biomed. Eng.* 28, 945–950.
- Sarmast, F., Kolli, A., Zaitsev, A., et al., 2003. Cholinergic atrial fibrillation: $I_{K, ACh}$ gradients determine unequal left/right atrial frequencies and rotor dynamics. *Cardiovasc. Res.* 59, 863–873.
- Sanders, P., Berenfeld, O., Hocini, M., et al., 2005. Spectral analysis identifies sites of high-frequency activity maintaining atrial fibrillation in humans. *Circulation* 112, 789–797.
- Seemann, G., Hoper, C., Sachse, F.B., Dossel, O., Holden, A.V., Zhang, H., 2006. Heterogeneous 3-dimensional anatomical and electrophysiological model of human atria. *Phil Trans. A* 364, 1465–1481.
- Spach, M.S., Dolber, P.C., Heidlage, J.F., 1989. Interaction of inhomogeneities of repolarization with anisotropic propagation in dog atria: a mechanism for both preventing and initiating reentry. *Circ. Res.* 65, 1612–1631.
- Stewart, S., Murphy, N., Walker, A., McGuire, A., McMurray, J.J.V., 2004. Cost of an emerging epidemic: an economic analysis of atrial fibrillation in the UK. *Heart* 90, 286–292.
- Weixue, L., Ling, X., 1996. Computer simulation of epicardial potentials using a heart-torso model with realistic geometry. *IEEE Trans. Biomed. Eng.* 43, 211–217.
- Wilders, R., 2007. Computer modelling of the sinoatrial node. *Med. Biol. Eng. Comput.* 45, 189–207.
- Yamamoto, M., Honjo, H., Niwa, R., Kodama, I., 1998. Low-frequency extracellular potentials recorded from the sinoatrial node. *Cardiovasc. Res.* 39, 360–372.
- Zhang, H., Holden, A.V., Kodama, I., Honjo, H., Lei, M., Varghese, T., Boyett, M.R., 2000. Mathematical models of action potentials in the periphery and center of the rabbit sinoatrial node. *Am. J. Physiol.* 279, H397–H421.